Preparation of Organometal Halide Perovskite Photonic Crystal Films for Potential Optoelectronic Applications

Stefan Schünemann[a], Kun Chen[a], Sarah Brittman[b], Erik Garnett[b], Harun Tüysüz[a]*

[a]Max-Planck-Institut für Kohlenforschung, Kaiser-Wilhelm-Platz 1, 45470 Mülheim an der Ruhr, Germany
[b]Center for Nanophotonics, FOM Institute AMOLF, Science Park 104, Amsterdam 1098 XG, The Netherlands
*Corresponding author: tueysuez@kofo.mpg.de

organometal halide perovskites, inverse opals, thin films, slow-light, photonic crystal

ABSTRACT: Herein, a facile method for the preparation of organometal halide perovskite (OHP) thin films in photonic crystal morphology is presented. The OHP photonic crystal thin films with controllable porosity and thicknesses between 2 and 6 µm were prepared on glass, FTO, and TiO_2 substrates by using a colloidal crystal of polystyrene microspheres as a template to form an inverse opal structure. The composition of OHP could be straightforwardly tuned by varying the halide anions. The obtained OHP inverse opal films possess large ordered domains with a periodic change of the refractive index, which results in pronounced photonic stop bands in the visible light range. By changing the diameter of the polystyrene microspheres, the position of the photonic stop band can be tuned through the visible spectrum. This developed methodology can be used as blueprint for the synthesis of various OHP films that could eventually be used as more effective light harvesting materials for diverse applications.

Introduction

Over the past years, organometal halide perovskites (OHPs) have attracted great interest in the fields of photovoltaics and optoelectronics.[1-6] The massive research activities on OHPs are due to not only their long carrier lifetimes[7] and diffusion lengths[8, 9], but also to high absorption coefficients at energies above the bandgap.[10] Furthermore, OHPs can be fabricated in a low-cost solution process and allow facile bandgap engineering by changing their composition.[11, 12]

Structures for OHP photovoltaic devices usually comprise flat and uniform thin films as the light-absorbing layer.[13-18] However, recently structured perovskite films drew considerable attention since control over the microstructure modifies electronic properties such as lateral conductivity, ionic conductivities, charge carrier separation rates, and emission wavelengths.[17, 19-24] The fabrication of perovskite materials in well-defined structure is challenging due to the rapid crystallization of the precursors and restructuring in the presence of trace water.[25] Inspired by colloidal crystal templating, our group recently published an innovative protocol for the synthesis of powdered OHPs in inverse opal (IO) morphology.[20] An IO is a three-dimensional (3D) photonic crystal that consists of a densely packed array of void spheres, which are surrounded by a solid material. The periodically changing refractive index creates a photonic stop band, which is - similar to a semiconductor's bandgap for electrons - a region in which electromagnetic waves cannot propagate.[26, 27] By tuning the lattice parameters (i. e. the size of the spherical voids), it is possible to tune the position of the stop band over the visible light spectrum. Since the group velocity is defined as the slope of the reduced frequency in the reciprocal space, the presence of a photonic stop band inherently implies a reduced group velocity at the edges of the photonic stop band. The reduced group velocity of photons (slow-light) can give rise to increased absorption of photons at the red edge of the photonic stop band in the high index medium.[26, 28-32] The position of the stop band can be calculated from the modified Bragg law and depends on the refractive index contrast between the voids and the surrounding material, the filling fractions of the materials, the lattice constant, and also on the angle of the incoming light relative to the crystal's orientation.[33]

Various studies show that the application of 3D photonic crystals of other materials such as TiO_2[29, 34-36], WO_3[28, 37], CuO[38], and various other metal oxides[39-43] increases the efficiency of solar cells and photoanodes owing to the slow-light effect and the anisotropic propagation of light. Due to the angle dependence of the stop band position, it is not sufficient to deposit powdered IO particles on a film, which results in randomly distributed crystal orientations. Instead, employing the increased absorption of photons by the slow-light effect of OHP IOs in light harvesting applications requires the same photonic crystal orientation over an entire sample, or at least an area as large as the incident beam. Consequently, the direct formation of thin IO films with a defined and constant orientation is more desirable than depositing randomly distributed IO powders. A particular challenge for the application of IOs in solar cells is the thickness control of IO films, especially when the efficiencies of OHP solar cells strongly depend on the thickness of the absorbing OHP layer.[16, 21, 44] In 2D photonic structures, such as a close packed monolayer of spheres, a change of the lattice constant also results in a change of the thickness.[21] In 3D photonic crystals, the lattice constant and thus the position of the photonic stop band can be varied without affecting the thickness of the photonic crystal.

To achieve enhanced solar cell efficiencies, the photonic stop band has to be tuned relative to the electronic bandgap of the semiconductor such that slow photons are present in the high index medium (i. e. the perovskite) at wavelengths at which the semiconductor only weakly absorbs photons, i.e. close to the bandgap energy. Thus, the photonic stopband needs to be at wavelengths slightly lower than the band edge.[26, 29] In addition to the advantage of the reduced group velocity of photons close to the photonic stop band, the colloidal crystal templating approach to fabricate structure-controlled OHP films offers advantages such as large surface area and short transport distances that could result in more efficient movement of charge carriers through the film, opening the possibility for new applications.[21] Furthermore, inverse opals and comparable photonic structures of other materials were also shown to increase the light extraction efficiency of various types of light emitting diodes by diffraction of waveguided light.[45-49] Since inverse opal photonic crystals can either enhance or suppress spontaneous emission by modifying the density of electromagnetic modes, such structures are also applicable as distributed feedback lasers[19,50-55], which have not yet been achieved for OHPs. In analogy to the directed flow of electrons through a wire, the waveguiding properties of inverse opals can also be applied to fabricate circuits for communication and processing.[32, 56] To the best of our knowledge, 3D organometal halide perovskite photonic crystal in thin film morphology have not yet been realized.

In this study, we report for the first time the fabrication of thickness-controlled methylammonium lead halide 3D photonic crystal thin films by a colloidal crystal templating route comprising PS opal formation via drop-casting, OHP infiltration via spin-coating, and template removal in toluene (**Figure 1**). By tuning the size of the polystyrene spheres hard template and the halide anions, a range of OHP photonic crystal films on various substrates with pronounced photonic stop bands could be fabricated.

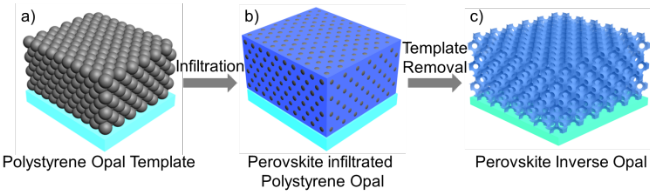

Figure 1: Schematic preparation route of OHP IO thin films including self-assembly of PS spheres via drop casting (a), Perovskite infiltration via spin-coating (b), and template removal with toluene (c).

Materials and Methods

Methods: All chemicals were analytical grade and used as received without further purification. Conductive fluorine doped tin oxide (FTO) substrates were purchased from Sigma Aldrich (8 Ω/sq).

Polystyrene synthesis: Polystyrene spheres were synthesized by a surfactant assisted emulsion polymerization approach modified from literature.[57] Briefly, 190 mL water was added to a 500 mL two necked round bottom flask equipped with a reflux condenser and Ar inlet. The water was stirred for 10 minutes at 80 °C and purged with argon before 20 mL of styrene (previously extracted 3 times with 1 M NaOH and 3 times with deionized water) were added. After the mixture reached a stable temperature of 80 °C, 617 mg sodium persulfate and 92.0 mg sodium dodecyl sulfate dissolved in 10 mL water were rapidly added to the mixture. The mixture was stirred for 5 h under Ar atmosphere. Subsequently, the white suspension was sedimented by centrifugation (30 min, 16500 rpm). The supernatant liquid was removed and the polystyrene spheres were re-dispersed in water via sonication. This process was repeated three times. Finally, the suspensions were diluted to 0.5 wt.-% polystyrene. By adjusting the stirring speed during polymerization, PS spheres with diameter of 205, 220, and 260 nm (from SEM) were obtained.

Methylammonium bromide[20]: 48 wt.% hydrobromic acid (20.4 mL, 180 mmol) was slowly added to a 33 wt% methylamine solution in ethanol (20.0 mL, 161 mmol) at 0 °C and stirred for 2 h in a 100 mL round bottomed flask. The solvent was removed by rotary evaporation at 60 °C. The obtained solid was washed with diethyl ether for 30 min and recrystallized from ethanol. Finally, the crystals were dried at 50 °C in a vacuum oven for 24 h.

Methylammonium iodide[20]*:* 57 wt.% hydroiodic acid (23.8 mL, 180 mmol) was slowly added to a 33 wt% methylamine solution in ethanol (20.0 mL, 161 mmol) at 0 °C and stirred for 2 h in a 100 mL round bottomed flask. The solvent was removed by rotary evaporation at 60 °C. The obtained solid was washed with diethyl ether for 30 min and recrystallized from ethanol. Finally, the crystals were dried at 50 °C in a vacuum oven for 24 h.

Methylammonium chloride[58]: 37 wt.% hydrochloric acid (15 mL, 180 mmol) was slowly added to a 33 wt% methylamine solution in methanol (20.0 mL, 161 mmol) at 0 °C and stirred for 2 h in a 100 mL round bottomed flask. The solvent was removed by rotary evaporation at 60 °C. The obtained solid was washed with diethyl ether for 30 min and recrystallized from ethanol. Finally, the crystals were dried at 0 °C in a vacuum oven for 24 h.

TiO_2 substrates[18]: FTO substrates were cleaned by sonication in acetone, isopropanol and water for 20 min each. Subsequently 0.15 M titanium diisopropoxide bis(acetylacetonate) (Sigma Aldrich, 75 wt.% in isopropanol) in 1-butanol was spin-coated on an FTO glass substrate at 700 rpm for 8 sec, 1000 rpm for 10 sec and 2000 rpm for 40 sec. Subsequently, the films were dried for 5 min at 125 °C and then calcined for 1 h at 550 °C.

PS opal films: PS opal films were prepared on 25x25 mm^2 glass and FTO/TiO_2 substrates previously cleaned by sonication in acetone, isopropanol and water for 20 min each. Hydrophilicity was achieved by immersing the clean glass slides in a freshly prepared piranha solution for at least 1 h. Subsequently, the glass slides were placed on a hot plate at 60 °C and 200 μL of a 0.5 % PS solution was dropped on the glass slide. Evaporation of the solvent leads to the self-assembly of the PS spheres in a closest packed array with the (111) surface parallel to the glass surface and a mean thickness of 2 μm. PS opal films with thicknesses of 3 and 6 μm were prepared by adjusting the volume of the polystyrene suspension to 300 and 600 mL, respectively. For comparison, a disordered opal like PS template was fabricated by mixing the three PS suspensions in equal volumetric amounts before drop casting.

Methylammonium lead halide inverse opal films: 150 µL of a 1 M methylammonium lead halide solution consisting of 1 M methylammonium halide and 1 M lead(II) halide in DMSO was dropped on the as prepared PS opal films and spun at 2000 rpm for 10 s. After drying at 60 °C for 1 h, the PS template was removed by immersing the film in toluene for one minute at room temperature.

Electron microscopy: Scanning electron microscopy (SEM) images were taken with Hitachi TM3030 and S-3500N electron microscopes.

X-ray diffraction: Wide angle X-ray diffraction patterns (XRD) were recorded at room temperature under grazing incidence on a Stoe theta/theta diffractometer in Bragg-Brentano geometry (Cu Kα ½ radiation). The measured patterns were evaluated qualitatively by comparison with entries from the ICDD-PDF-2 powder pattern database or with calculated patterns using literature structure data.

Microscale reflectance and transmittance/scattering[59]: Microscale reflectance and transmittance/scattering measurements were made using a home-built optical setup. The sample was illuminated with modulated monochromatic light, and the incident, reflected, and transmitted/scattered beams were measured via lock-in detection (Stanford Research Systems, SR830) on three different amplified photodetectors (Thorlabs PDA100A). A supercontinuum light source (Fianium WL-SC390-3) was sent through an acousto-optic tunable filter (Fianium AOTF-V1-N1) to produce monochromatic (FWHM 3 nm) light tunable from 400-750 nm. The wavelengths were measured using an OceanOptics USB4000 spectrometer. Light from the laser was rotated to vertical polarization using a half-wave plate and sent through a beamsplitter (Thorlabs, CM1-BS013): one branch went directly to a photodetector to measure the incident power and the other branch was focused down onto the sample using an objective with low chromatic aberration (Mitutoyo M Plan Apo NUV 50X, NA 0.42). The sample was mounted inside a 2-inch integrating sphere. The light reflected from the sample passed back through the objective and was directed by the beamsplitter to the reflectance photodetector. The light transmitted and scattered by the sample was collected by the photodetector mounted on the integrating sphere and screened from direct incidence by a baffle. The photodetectors used to measure reflectance and incident power were adjusted at slight angles to the incident beam avoid any back-reflections within the optical system. Calibration of the reflectance photodetector was performed using a protected silver mirror (Thorlabs, PF10-S303-P01) and assuming the company's reflectance values published on their website. Because of the small size of the integrating sphere and high absorptance of the samples, measurements of the transmitted and scattered light were corrected[60] for absorption of the diffuse light within the integrating sphere by measuring the absorptance (a) when the laser missed the sample inside the integrating sphere and using the following formula:

$$T_{corrected} = \frac{1}{1-a} T_{measured}$$

The total absorptance (A) is then $A=1-R-T_{corrected}$.

Angle-dependent transmittance: Angle-dependent transmittance of polystyrene opal films at different angles were recorded with a Varian Cary 4000 spectrometer equipped with a home-built sample holder, which allows the rotation of the films in 5° increments.

Diffuse reflectance: UV-Vis diffuse reflectance spectra of $MAPbBr_3$ inverse opals prepared on different substrates were conducted on a Varian Cary 4000 spectrometer equipped with praying mantis setup. MgO nanoparticles were used as a reference.

Angle-dependent reflectance: Angle-dependent reflectance spectra were recorded from 0° to 60° in steps of 2.5° in theta/theta geometry.

Results and Discussion

OHP inverse opal thin films were prepared by a colloidal crystal templating method, using polystyrene (PS) spheres as a hard template which was self-assembled by a facile drop casting method, followed by infiltration with the OHP precursor in DMSO and subsequent template removal in toluene.[20] To elucidate the effect of the photonic stopband's position on the optical properties of $MAPbBr_3$, PS opals with various sphere diameters of 205, 220, and 260 nm were prepared on glass substrates. The PS diameters were chosen to give photonic stop bands of the $MAPbBr_3$ inverse opals above, overlapped with, and below the bandgap energy of $MAPbBr_3$, respectively. The prepared opals are close packed with the (111) surface parallel to the glass surface and possess large ordered domains with dimensions of 10's of µm by 10 µm, as representative SEM images show (**Figure S1**). Unlike most reported protocols for preparing PS opals that either are very time consuming[61] or yield thick films[62] between 10's and 100's of µm with large thickness modulations[61, 63], our protocol, which is a modification from literature[57], employs surfactant assisted polymerization of PS and allows the formation of homogeneously thin films with controllable thicknesses between 2 and 6 µm within minutes via drop casting. The thickness of the opal can easily be tuned by adjusting the volume of the PS suspension used for drop casting (**Figure S2**).

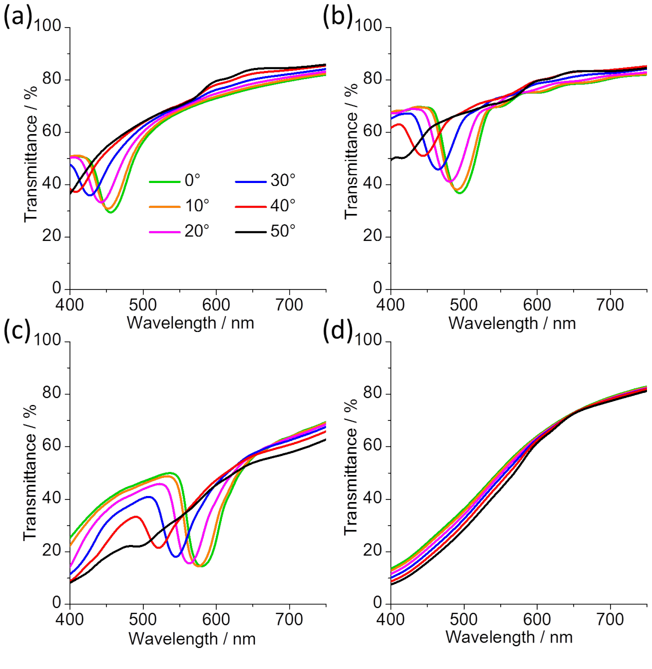

Figure 2: Transmittance spectra of 205-PS (a), 220-PS (b), 260-PS (c), and Mix-PS (d) at different angles of the incident light normal to the film surface. Insets show the square of the wavelength at the stop band maximum as a function of the square sine of the incident light (black circles) together with linear regression lines (red line).

To elucidate the effect of periodic contrast of the refractive index on the optical properties of the IO perovskite films, a disordered opal-like PS film was synthesized by drop casting a PS suspension consisting of equal amounts of the three PS suspensions with differently sized PS spheres. In the following, the PS opal films are named 205-PS, 220-PS, 260-PS, and Mix-PS, according to the PS diameter.

The close packed array of PS spheres results in a periodic contrast of the refractive index with a periodicity on the order of half a wavelength of visible light, which, according to the modified Bragg law[43], results in a photonic stop band in the visible light. The ultraviolet-visible (UV-Vis) transmittance spectra of the PS opal films (**Figure 2**), 205-PS, 220-PS, and 260-PS show reduced transmittances at around 455, 490, and 580 nm at normal incidence, respectively. The observed dips in transmittance are the result of the photonic stop band of the (111) plane of the PS opals.

The stop band position of the (111) plane of close packed photonic structures such as opals and inverse opals can be calculated according to the modified Bragg law (**Equation 1**)[43], where D is the diameter of the PS spheres, f_1 is the filling fraction of component 1, which in the case of close packed structures is 0.76. n_1 and n_2 are the refractive indices of the components and θ is the angle of the incident light perpendicular to the (111) surface. Transmittance measurements at different angles of the incident light (θ) show a hypsochromic (blue) shift of the stop band position (**Figure 2**). **Figure S3** shows the linear relation between the square of the stop band maximum wavelength λ_{max}^2 and $sin^2(\theta)$, which is in accordance with the modified Bragg law (**Equation 1**).

$$\lambda_{max} = \frac{2\sqrt{6}}{3} D \sqrt{f_1 {n_1}^2 - (1-f_1){n_2}^2 - sin^2(\theta)} \qquad (1)$$

For comparison, an opal like sample (Mix-PS), consisting of equal amounts of PS spheres with sizes of 205, 220, and 260 nm, was prepared, too. The different sizes of the PS spheres inhibit the formation of an ordered array of PS spheres (**Figure S1**), which in turn inhibits the formation of a photonic stop band. **Figure 2d** shows the angle dependent transmittance spectra of Mix-PS which, as expected, does not possess a photonic stop band because of the absence of ordering in the structure. Instead, the transmittance of Mix-PS is strongly reduced at short wavelengths because of scattering by the disordered structure.

The prepared PS opal films were used as templates to prepare methylammonium lead halide photonic crystal thin films which are also expected to possess a photonic stop band. For this, the templates 205-PS, 220-PS, 260-PS, and Mix-PS were infiltrated with a 1 M $MAPbBr_3$ precursor solution consisting of 1 M methylammonium bromide and 1 M $PbBr_2$ in DMSO via spin-coating followed by drying at 60 °C in ambient atmosphere. After drying and crystallization, the PS templates were removed selectively by immersing the samples in toluene at room temperature in air. The obtained $MAPbBr_3$ IO films are labelled as 205-$MAPbBr_3$, 220-$MAPbBr_3$, 260-$MAPbBr_3$, and Mix-$MAPbBr_3$, based on the size of the PS spheres. Representative SEM images (**Figure 3**) show the well-ordered IO structures of 205-$MAPbBr_3$, 220-$MAPbBr_3$, 260-$MAPbBr_3$ and the disordered structure of Mix-$MAPbBr_3$ (lower magnifications are given in **Figure S4**). The 3D opal structure of the PS template is well replicated by the perovskite material, which forms a honeycomb-like IO lattice in three dimensions. The cross-sectional SEM image of 220-$MAPbBr_3$ in **Figure 3e** shows that PS is completely removed in all layers of the IO upon treatment in toluene.

For photovoltaic application of OHP IO films, it is essential to fabricate IO films on conductive substrates such as fluorine doped tin oxide (FTO) and TiO_2 deposited on FTO. We therefore fabricated 220-$MAPbBr_3$ by the identical method on these substrates as well. Cross sectional SEM images of 220-$MAPbBr_3$ prepared on FTO and TiO_2 deposited on FTO show a well ordered IO structure and good contact to the substrates (**Figure S5**). Furthermore, the IO films prepared on these substrates possess a pronounced photonic band gap with, compared to IO films prepared on glass, similar position and reflectivity, as diffuse reflectance spectra show (**Figure S6**). The high reflectivities of approximately 55 % indicate the presence of well-ordered IO domains for all three substrates.

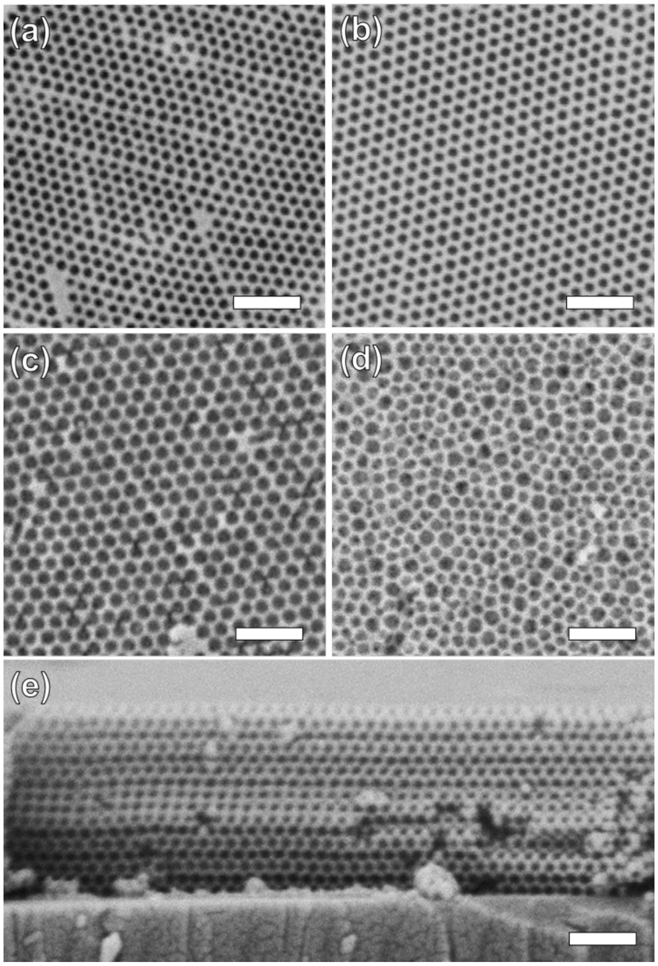

Figure 3: Representative SEM images of 205-$MAPbBr_3$ (a), 220-$MAPbBr_3$ (b), 260-$MAPbBr_3$(c), and Mix-$MAPbBr_3$ (d) and cross-sectional image of 3 µm thick 220-$MAPbBr_3$ (e). Scale bar in each image is 1 µm.

The PS sphere sizes that were employed in this study were chosen to match the bandgap energy of $MAPbBr_3$ to make use of the slow-light effect at the bandgap region of $MAPbBr_3$. However, the synthetic protocol can generally be applied to other OHPs. To show the applicability of this method for the preparation of other OHP IO films, 220-PS was infiltrated with 1 M solutions of $MAPbCl_3$, $MAPbCl_{1.5}I_{1.5}$ and $MAPbI_3$ in DMSO by the same method that is aforementioned. As SEM images (**Figure S7**) show, also these perovskites form well-ordered IO films with large ordered domains. Grazing incidence X-ray diffraction analyses confirm the cubic phase of 220-MAPbBr$_3$, 220-MAPbCl$_3$ and the tetragonal phase of 220-MAPbI$_3$. The diffractogram of 220-MAPbCl$_{1.5}$I$_{1.5}$ shows a superposition of 220-MAPbCl$_3$ and 220-MAPbI$_3$, which indicates the coexistence of both species in the sample (**Figure 4**).

The fabrication of IOs of most semiconductor materials as TiO$_2$[64], WO$_3$[28], and BiVO$_4$[40], requires high temperature treatment which leads to shrinkage of the structure and consequently to the destruction of the periodic arrangement of the IO structure, which in turn strongly inhibits the formation of a photonic stop band. However, the crystallization of OHPs does not require treatment at high temperatures and the template can be efficiently removed by a solvent at room temperature. Consequently, no shrinkage of the structure occurs. This is evident from the linear shrinkage of the sphere diameter which is below 1 %.

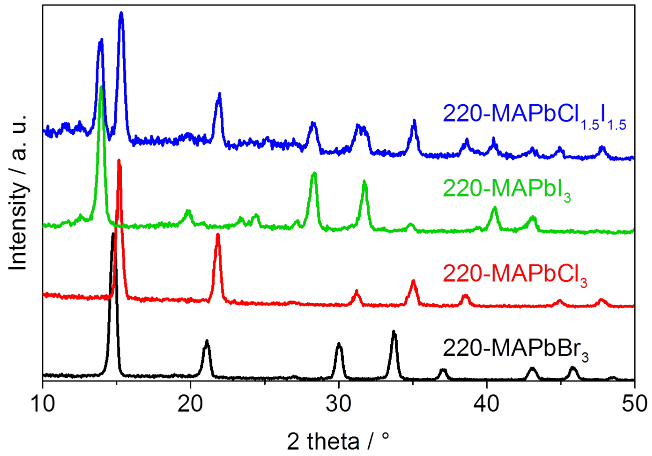

Figure 4: Grazing incidence X-ray diffraction pattern of 220-MAPbBr$_3$, 220-MAPbCl$_3$, 220-MAPbI$_3$, and 220-MAPbCl$_{1.5}$I$_{1.5}$ the spectra are offset along the y-axis for clarity.

The absence of shrinkage yields highly ordered inverse opals displaying pronounced photonic stop bands above, overlapped with, and below the bandgap energy of MAPbBr$_3$ at around 435, 545, and 640 nm, respectively (**Figure 5a-c**). In contrast, Mix-MAPbBr$_3$ does, not show a photonic stop band (**Figure 5d**). Compared to the other IOs, 205-MAPbBr$_3$ possesses a less pronounced reflectance peak, which can be attributed to the strong absorbance of MAPbBr$_3$ in this spectral region, which prohibits light propagation through deeper layers of the IO structure. Furthermore, light reflected by the photonic stop band at 435 nm is being absorbed by MAPbBr$_3$ before it can exit the material

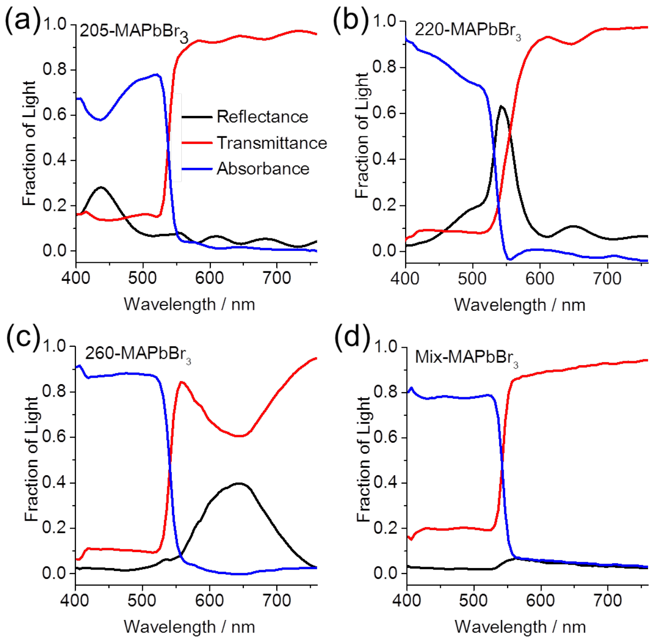

Figure 5: Microscale reflectance, transmittance/scattering, and absorptance spectra of 205-MAPbBr$_3$ (a), 220-MAPbBr$_3$ (b), 260-MAPbBr$_3$ (c), and Mix-MAPbBr$_3$ (d) measured in an integrating sphere

In devices, enhanced incident photon-to-current efficiency (IPCE) is expected when the photonic stop band is slightly blue-shifted from the bandgap energy so that slow-light is present at the weakly absorbing bandgap region of the high index medium. The bandgap energy of MAPbBr$_3$ is 2.2-2.3 eV, i.e. 565-540 nm. Thus, at normal incidence 220-MAPbBr$_3$ possesses a photonic stop band within the bandgap energy. Angle-dependent reflectance measurements of this sample were recorded between 0 and 60° at 2.5° intervals and show the expected blue-shift of the photonic stopband at increasing angles of the incident light (**Figure 6a**). The stop band position hypsochromically shifts from 547 nm at normal incidence to 535 nm at an angle of 60°, meaning that the stop band shifts through the bandgap energy of MAPbBr$_3$. **Figure 6b** shows the linear dependence between the square of the stop band wavelength and the square sine of the incident angle, as expected from the modified Bragg law.

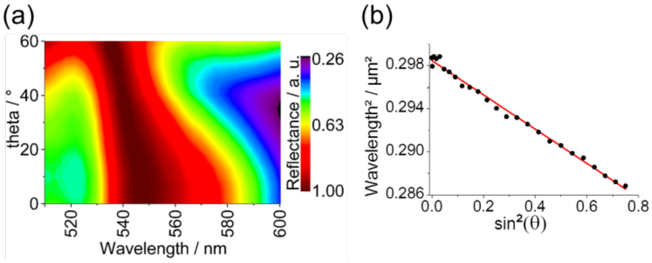

Figure 6: Angle-dependent reflectance of 220-MAPbBr$_3$ (normalized to the reflectance at the stopband maximum) (a) and linearized plot of the stop band maximum between 0° and 60° with linear regression line (red) (b).

Conclusion

In summary, we have demonstrated a facile protocol to fabricate methylammonium lead halide inverse opal thin films with controllable thicknesses comparable to that relevant for organometal lead halide solar cells on glass, FTO, and TiO$_2$

substrates. The prepared 3D photonic crystals possess large ordered domains and pronounced photonic stop bands whose position can be tuned by adjusting the diameter of the polystyrene spheres employed as the template and by changing the angle of the incident light, as angle-dependent reflectance measurements show. By changing the halide groups, the composition, crystal structure and bandgap of the perovskite photonic crystal thin films could be also straightforwardly tuned. The prepared inverse opal organometal halide perovskite photonic crystal films could lead to improved perovskite based solar cells by replacing the dense perovskite layer by an inverse opal structured layer to employ the slow-light effect for light harvesting applications.

ASSOCIATED CONTENT

SEM images of 205-PS, 220-PS, 260-PS, and Mix-PS, cross section SEM of 220-PS with different thicknesses, angle dependent stopband maximum position of PS opal films, representative SEM images of MAPbBr$_3$ inverse opals, cross section SEM images of 220-MAPbBr$_3$ on FTO and TiO$_2$/FTO substrates, diffuse reflectance UV-Vis spectra of 220-MAPbBr$_3$ on glass, FTO, and TiO$_2$/FTO, XRD patterns of 220-MAPbBr$_3$, 220-MAPbCl$_3$, 220-MAPbI$_3$, and 220-MAPbCl$_{1.5}$I$_{1.5}$
This material is available free of charge via the Internet at http://pubs.acs.org.

ACKNOWLEDGMENT

This work was supported by the MAXNET Energy consortium of Max Planck Society, the Cluster of Excellence RESOLV (EXC 1069) funded by the Deutsche Forschungsgemeinschaft (DFG) and Fonds der Chemischen Industrie (FCI). This work is part of the research program of the Foundation for Fundamental Research on Matter (FOM), The authors acknowledge financial support from the European Research Council under the European Union's Seventh Framework Programme (FP/2007-2013)/ERC Grant Agreement no. 337328, "Nano-Enabled PV," and from an industrial partnership between Philips and FOM. The authors are grateful for angle dependent reflection measurements by Verena Neder from the group of Prof. Dr. Albert Polman at the FOM Institute AMOLF and fruitful discussion with Dr. Frank Marlow. The authors would like to thank Silvia Palm for SEM images, and Christian Belting for general support in the laboratory.

ABBREVIATIONS

PS, polystyrene; MA, methylammonium; IO, inverse opal; OHP organometal halide perovskite

REFERENCES

(1) Stranks, S. D.; Nayak, P. K.; Zhang, W.; Stergiopoulos, T.; Snaith, H. J., Formation of Thin Films of Organic-Inorganic Perovskites for High-Efficiency Solar Cells. Angew. Chem. Int. Ed. 2015, 54, 3240-3248.

(2) Jung, H. S.; Park, N.-G., Perovskite Solar Cells: From Materials to Devices. Small 2015, 11, 10-25.

(3) Gao, P.; Grätzel, M.; Nazeeruddin, M. K., Organohalide Lead Perovskites for Photovoltaic Applications. Energ. Environ. Sci. 2014, 7, 2448-2463.

(4) Green, M. A.; Ho-Baillie, A.; Snaith, H. J., The Emergence of Perovskite Solar Cells. Nat. Photon. 2014, 8, 506-514.

(5) Ke, W.; Fang, G.; Wang, J.; Qin, P.; Tao, H.; Lei, H.; Liu, Q.; Dai, X.; Zhao, X., Perovskite Solar Cell with an Efficient TiO2 Compact Film. ACS Appl. Mater. Interfaces 2014, 6, 15959-15965.

(6) Shi, J.; Luo, Y.; Wei, H.; Luo, J.; Dong, J.; Lv, S.; Xiao, J.; Xu, Y.; Zhu, L.; Xu, X.; Wu, H.; Li, D.; Meng, Q., Modified Two-Step Deposition Method for High-Efficiency TiO2/CH3NH3PbI3 Heterojunction Solar Cells. ACS Appl. Mater. Interfaces 2014, 6, 9711-9718.

(7) Wehrenfennig, C.; Eperon, G. E.; Johnston, M. B.; Snaith, H. J.; Herz, L. M., High Charge Carrier Mobilities and Lifetimes in Organolead Trihalide Perovskites. Adv. Mater. 2014, 26, 1584-1589.

(8) Stranks, S. D.; Eperon, G. E.; Grancini, G.; Menelaou, C.; Alcocer, M. J. P.; Leijtens, T.; Herz, L. M.; Petrozza, A.; Snaith, H. J., Electron-Hole Diffusion Lengths Exceeding 1 Micrometer in an Organometal Trihalide Perovskite Absorber. Science 2013, 342, 341-344.

(9) Colella, S.; Mosconi, E.; Fedeli, P.; Listorti, A.; Gazza, F.; Orlandi, F.; Ferro, P.; Besagni, T.; Rizzo, A.; Calestani, G.; Gigli, G.; De Angelis, F.; Mosca, R., MAPbl(3-x)Cl-x Mixed Halide Perovskite for Hybrid Solar Cells: The Role of Chloride as Dopant on the Transport and Structural Properties. Chem. Mater. 2013, 25, 4613-4618.

(10) Yin, W.-J.; Shi, T.; Yan, Y., Unique Properties of Halide Perovskites as Possible Origins of the Superior Solar Cell Performance. Adv. Mater. 2014, 26, 4653-4658.

(11) Xing, G.; Mathews, N.; Lim, S. S.; Yantara, N.; Liu, X.; Sabba, D.; Grätzel, M.; Mhaisalkar, S.; Sum, T. C., Low-Temperature Solution-Processed Wavelength-Tunable Perovskites for Lasing. Nat. Mater. 2014, 13, 476-480.

(12) Chen, K.; Deng, X.; Goddard, R.; Tüysüz, H., Pseudomorphic Transformation of Organometal Halide Perovskite Using the Gaseous Hydrogen Halide Reaction. Chem. Mater. 2016, 28, 5530-5537.

(13) Kim, J. H.; Williams, S. T.; Cho, N.; Chueh, C. C.; Jen, A. K. Y., Enhanced Environmental Stability of Planar Heterojunction Perovskite Solar Cells Based on Blade-Coating. Adv. Energy Mater. 2015, 5, 1401229.

(14) Docampo, P.; Hanusch, F. C.; Stranks, S. D.; Doblinger, M.; Feckl, J. M.; Ehrensperger, M.; Minar, N. K.; Johnston, M. B.; Snaith, H. J.; Bein, T., Solution Deposition-Conversion for Planar Heterojunction Mixed Halide Perovskite Solar Cells. Adv. Energy Mater. 2014, 4, 1400355.

(15) Nan, F.; Kang, Z. H.; Wang, J. L.; Shen, M. R.; Fang, L., Carbon Quantum Dots Coated BiVO4 Inverse Opals for Enhanced Photoelectrochemical Hydrogen Generation. Appl. Phys. Lett. 2015, 106, 153901.

(16) Shi, J.; Luo, Y.; Wei, H.; Luo, J.; Dong, J.; Lv, S.; Xiao, J.; Xu, Y.; Zhu, L.; Xu, X.; Wu, H.; Li, D.; Meng, Q., Modified Two-Step Deposition Method for High-Efficiency TiO2/CH3NH3PbI3 Heterojunction Solar Cells. ACS Appl. Mater. Interfaces 2014, 6, 9711-9718.

(17) Dou, L.; Wong, A. B.; Yu, Y.; Lai, M.; Kornienko, N.; Eaton, S. W.; Fu, A.; Bischak, C. G.; Ma, J.; Ding, T.; Ginsberg, N. S.; Wang, L.-W.; Alivisatos, A. P.; Yang, P., Atomically Thin Two-Dimensional Organic-Inorganic Hybrid Perovskites. Science 2015, 349, 1518-1521.

(18) Ahn, N.; Son, D.-Y.; Jang, I.-H.; Kang, S. M.; Choi, M.; Park, N.-G., Highly Reproducible Perovskite Solar Cells with Average Efficiency of 18.3% and Best Efficiency of 19.7% Fabricated via Lewis Base Adduct of Lead(II) Iodide. J. Am. Chem. Soc. 2015, 137, 8696-8699.

(19) Saliba, M.; Wood, S. M.; Patel, J. B.; Nayak, P. K.; Huang, J.; Alexander-Webber, J. A.; Wenger, B.; Stranks, S. D.; Horantner, M. T.; Wang, J. T.; Nicholas, R. J.; Herz, L. M.; Johnston, M. B.; Morris, S. M.; Snaith, H. J.; Riede, M. K., Structured Organic-Inorganic Perovskite toward a Distributed Feedback Laser. Adv. Mater. 2016, 28, 923-929.

(20) Chen, K.; Tüysüz, H., Morphology-Controlled Synthesis of Organometal Halide Perovskite Inverse Opals. Angew. Chem. Int. Ed. 2015, 54, 13806-13810.

(21) Meng, K.; Gao, S.; Wu, L.; Wang, G.; Liu, X.; Chen, G.; Liu, Z.; Chen, G., Two-Dimensional Organic-Inorganic Hybrid Perovskite Photonic Films. Nano Lett. 2016, 16, 4166-4173.

(22) Di, D.; Musselman, K. P.; Li, G.; Sadhanala, A.; Ievskaya, Y.; Song, Q.; Tan, Z. K.; Lai, M. L.; MacManus-Driscoll, J. L.; Greenham, N. C.; Friend, R. H., Size-Dependent Photon Emission from Organometal Halide Perovskite Nanocrystals Embedded in an Organic Matrix. J. Phys. Chem. Lett. 2015, 6, 446-450.

(23) Chang, C.-Y.; Chu, C.-Y.; Huang, Y.-C.; Huang, C.-W.; Chang, S.-Y.; Chen, C.-A.; Chao, C.-Y.; Su, W.-F., Tuning Perovskite Morphology by Polymer Additive for High Efficiency Solar Cell. ACS Appl. Mater. Interfaces 2015, 7, 4955-4961.

(24) Zhang, F.; Yang, X.; Wang, H.; Cheng, M.; Zhao, J.; Sun, L., Structure Engineering of Hole-Conductor Free Perovskite-Based Solar Cells with Low-Temperature-Processed Commercial Carbon Paste As Cathode. ACS Appl. Mater. Interfaces 2014, 6, 16140-16146.

(25) Christians, J. A.; Miranda Herrera, P. A.; Kamat, P. V., Transformation of the Excited State and Photovoltaic Efficiency of CH3NH3PbI3 Perovskite upon Controlled Exposure to Humidified Air. J. Am. Chem. Soc. 2015, 137, 1530-1538.

(26) Curti, M.; Schneider, J.; Bahnemann, D. W.; Mendive, C. B., Inverse Opal Photonic Crystals as a Strategy to Improve Photocatalysis: Underexplored Questions. J. Phys. Chem. Lett. 2015, 6, 3903-3910.

(27) Wang, D. Y.; Rogach, A. L.; Caruso, F., Composite Photonic Crystals from Semiconductor Nanocrystal/Polyelectrolyte-Coated Colloidal Spheres. Chem. Mater. 2003, 15, 2724-2729.

(28) Chen, X.; Ye, J.; Ouyang, S.; Kako, T.; Li, Z.; Zou, Z., Enhanced Incident Photon-to-Electron Conversion Efficiency of Tungsten Trioxide Photoanodes based on 3D-Photonic Crystal Design. ACS Nano 2011, 5, 4310-4318.

(29) Chen, J. I. L.; von Freymann, G.; Choi, S. Y.; Kitaev, V.; Ozin, G. A., Amplified Photochemistry with Slow Photons. Adv. Mater. 2006, 18, 1915-1519.

(30) Nishimura, S.; Abrams, N.; Lewis, B. A.; Halaoui, L. I.; Mallouk, T. E.; Benkstein, K. D.; van de Lagemaat, J.; Frank, A. J., Standing Wave Enhancement of Red Absorbance and Photocurrent in Dye-Sensitized Titanium Dioxide Photoelectrodes Coupled to Photonic Crystals. J. Am. Chem. Soc. 2003, 125, 6306-6310.

(31) Imhof, A.; Vos, W. L.; Sprik, R.; Lagendijk, A., Large Dispersive Effects Near the Band Edges of Photonic Crystals. Phys. Rev. Lett. 1999, 83, 2942-2945.

(32) Armstrong, E.; O'Dwyer, C., Artificial Opal Photonic Crystals and Inverse Opal Structures - Fundamentals and Applications from Optics to Energy Storage. J. Mater. Chem. C 2015, 3, 6109-6143.

(33) Marlow, F.; Muldarisnur; Sharifi, P.; Brinkmann, R.; Mendive, C., Opals: Status and Prospects. Angew. Chem. Int. Ed. 2009, 48, 6212-6233.

(34) Sordello, F.; Duca, C.; Maurino, V.; Minero, C., Photocatalytic Metamaterials: TiO2 Inverse Opals. Chem. Commun. 2011, 47, 6147-6149.

(35) Han, S. H.; Lee, S.; Shin, H.; Jung, H. S., A Quasi-Inverse Opal Layer Based on Highly Crystalline TiO2 Nanoparticles: A New Light-Scattering Layer in Dye-Sensitized Solar Cells. Adv. Energy Mater. 2011, 1, 546-550.

(36) Guo, M.; Yong, Z.; Xie, K.; Lin, J.; Wang, Y.; Huang, H., Enhanced Light Harvesting in Dye-Sensitized Solar Cells Coupled with Titania Nanotube Photonic Crystals: A Theoretical Study. ACS Appl. Mater. Interfaces 2013, 5, 13022-13028.

(37) Kim, J. K.; Moon, J. H.; Lee, T. W.; Park, J. H., Inverse Opal Tungsten Trioxide Films with Mesoporous Skeletons: Synthesis and Photoelectrochemical Responses. Chem. Commun. 2012, 48, 11939-11941.

(38) Yantara, N.; Pham, T. T.; Boix, P. P.; Mathews, N., Modulating Light Propagation in ZnO-Cu2O-Inverse Opal Solar Cells for Enhanced Photocurrents. Phys. Chem. Chem. Phys. 2015, 17, 21694-21701.

(39) Waterhouse, G. I. N.; Metson, J. B.; Idriss, H.; Sun-Waterhouse, D., Physical and Optical Properties of Inverse Opal CeO2 Photonic Crystals. Chem. Mater. 2008, 20, 1183-1190.

(40) Zhou, M.; Bao, J.; Xu, Y.; Zhang, J.; Xie, J.; Guan, M.; Wang, C.; Wen, L.; Lei, Y.; Xie, Y., Photoelectrodes Based upon Mo: BiVO4 Inverse Opals for Photoelectrochemical Water Splitting. Acs Nano 2014, 8, 7088-7098.

(41) Zhang, L.; Baumanis, C.; Robben, L.; Kandiel, T.; Bahnemann, D., Bi2WO6 Inverse Opals: Facile Fabrication and Efficient Visible-Light-Driven Photocatalytic and Photoelectrochemical Water-Splitting Activity. Small 2011, 7, 2714-2720.

(42) Zhou, M.; Bao, J.; Xu, Y.; Zhang, J.; Xie, J.; Guan, M.; Wang, C.; Wen, L.; Lei, Y.; Xie, Y., Photoelectrodes Based upon Mo:BiVO4 Inverse Opals for Photoelectrochemical Water Splitting. ACS Nano 2014, 8, 7088-7098.

(43) Schroden, R. C.; Al-Daous, M.; Blanford, C. F.; Stein, A., Optical Properties of Inverse Opal Photonic Crystals. Chem. Mater. 2002, 14, 3305-3315.

(44) Liu, T. F.; Liu, L. F.; Hu, M.; Yang, Y.; Zhang, L. J.; Mei, A. Y.; Han, H. W., Critical Parameters in TiO2/ZrO2/Carbon-Based Mesoscopic Perovskite Solar Cell. J. Power Sources 2015, 293, 533-538.

(45) Hyun, W. J.; Lee, H. K.; Oh, S. S.; Hess, O.; Choi, C. G.; Im, S. H.; Park, O. O., Two-Dimensional TiO2 Inverse Opal with a Closed Top Surface Structure for Enhanced Light Extraction from Polymer Light-Emitting Diodes. Adv. Mater. 2011, 23, 1846-1850.

(46) Jeon, S.; Jeong, J. H.; Song, Y. S.; Jeong, W. I.; Kim, J. J.; Youn, J. R., Vacuum Nano-Hole Array Embedded Organic Light Emitting Diodes. Nanoscale 2014, 6, 2642-2648.

(47) Park, H. K.; Yoon, S. W.; Choi, D. Y.; Do, Y. R., Fabrication of Wafer-Scale TiO2 Nanobowl Arrays via a Scooping Transfer of Polystyrene Nanospheres and Atomic Layer Deposition for their Application in Photonic Crystals. J. Mater. Chem. C 2013, 1, 1732-1738.

(48) Wang, J.; Shen, H. X.; Wang, C. F.; Chen, S., Multifunctional Ionomer-Derived Honeycomb-Patterned Architectures and their Performance in Light Enhancement of Light-Emitting Diodes. J. Mater. Chem. 2012, 22, 4089-4096.

(49) Hyun, W. J.; Lee, H. K.; Im, S. H.; Park, O. O., Two-Dimensional TiO2 Honeycomb Structure for Enhanced Light Extraction from Polymer Light-Emitting Diodes. J. Nanosci. Nanotechnol. 2014, 14, 8411-8415.

(50) Han, S. G.; Lim, J.; Shin, J.; Lee, S.-M.; Park, T.; Yoon, J.; Woo, K.; Lee, H.; Lee, W., Optically Pumped Distributed Feedback Dye Lasing with Slide-Coated TiO2 Inverse-Opal Slab as Bragg Reflector. Opt. Letters 2014, 39, 4743-4746.

(51) Nishijima, Y.; Joudkazis, S., Optical Characterization and Lasing in Three-Dimensional Opal-Structures. Front. Mater. 2015, 2, 1-10.

(52) Nishijima, Y.; Ueno, K.; Juodkazis, S.; Mizeikis, V.; Fujiwara, H.; Sasaki, K.; Misawa, H., Lasing with well-Defined Cavity Modes in Dye-Infiltrated Silica Inverse Opals. Opt. Express 2009, 17, 2976-2983.

(53) Mekis, A.; Meier, M.; Dodabalapur, A.; Slusher, R. E.; Joannopoulos, J. D., Lasing Mechanism in Two-Dimensional Photonic Crystal Lasers. Appl. Phys. A 1999, 69, 111-114.

(54) Imada, M.; Chutinan, A.; Noda, S.; Mochizuki, M., Multidirectionally Distributed Feedback Photonic Crystal Lasers. Phys. Rev. B 2002, 65, 195306.

(55) Misawa, H.; Nishijima, Y.; Ueno, K.; Juodkazis, S.; Mizeikis, V.; Maeda, M.; Minaki, M., Tunable Single-Mode Photonic Lasing from Zirconia Inverse Opal Photonic Crystals. Opt. Express 2008, 16, 13676-13684.

(56) Lopez, C., Materials Aspects of Photonic Crystals. Adv. Mater. 2003, 15, 1679-1704.

(57) Chiappini, A.; Armellini, C.; Chiasera, A.; Ferrari, M.; Fortes, L.; Goncalves, M. C.; Guider, R.; Jestin, Y.; Retoux, R.;

Conti, G. N.; Pelli, S.; Almeida, R. M.; Righini, G. C., An Alternative Method to Obtain Direct Opal Photonic Crystal Structures. J. Non-Cryst. Solids 2009, 355, 1167-1170.

(58) Park, B. W.; Jain, S. M.; Zhang, X.; Hagfeldt, A.; Boschloo, G.; Edvinsson, T., Resonance Raman and Excitation Energy Dependent Charge Transfer Mechanism in Halide-Substituted Hybrid Perovskite Solar Cells. ACS Nano 2015, 9, 2088-2101.

(59) Brittman, S.; Garnett, E. C., Measuring n and k at the Microscale in Single Crystals of CH3NH3PbBr3 Perovskite. J. Phys. Chem. C 2016, 120, 616-620.

(60) deMello, J. C.; Wittmann, H. F.; Friend, R. H., An Improved Experimental Determination of External Photoluminescence Quantum Efficiency. Adv. Mater. 1997, 9, 230-232.

(61) Teh, L. K.; Tan, N. K.; Wong, C. C.; Li, S., Growth Imperfections in Three-Dimensional Colloidal Self-Assembly. Appl. Phys. A 2005, 81, 1399-1404.

(62) Wang, J. X.; Wen, Y. Q.; Ge, H. L.; Sun, Z. W.; Zheng, Y. M.; Song, Y. L.; Jiang, L., Simple Fabrication of Full Color Colloidal Crystal Films with Tough Mechanical Strength. Macromol. Chem. Physic. 2006, 207, 596-604.

(63) Hartsuiker, A.; Vos, W. L., Structural Properties of Opals Grown with Vertical Controlled Drying. Langmuir 2008, 24, 4670-4675.

(64) Jia, F.; Sun, W.; Zhang, J. H.; Li, Y. F.; Yang, B., A Facile Approach to Fabricate Three-Dimensional Ordered Macroporous Rutile Titania at Low Calcination Temperature. J. Mater. Chem. 2012, 22, 2435-2441.

Preparation of Organometal Halide Perovskite Photonic Crystal Films

S. Schünemann[a], K. Chen[a], S. Brittman[b], E. Garnett[b], H. Tüysüz[a]*

[a] Max-Planck-Institut für Kohlenforschung, Kaiser-Wilhelm-Platz 1, 45470 Mülheim an der Ruhr, Germany

[b] Center for Nanophotonics, FOM Institute AMOLF, Science Park 104, Amsterdam 1098 XG, The Netherlands

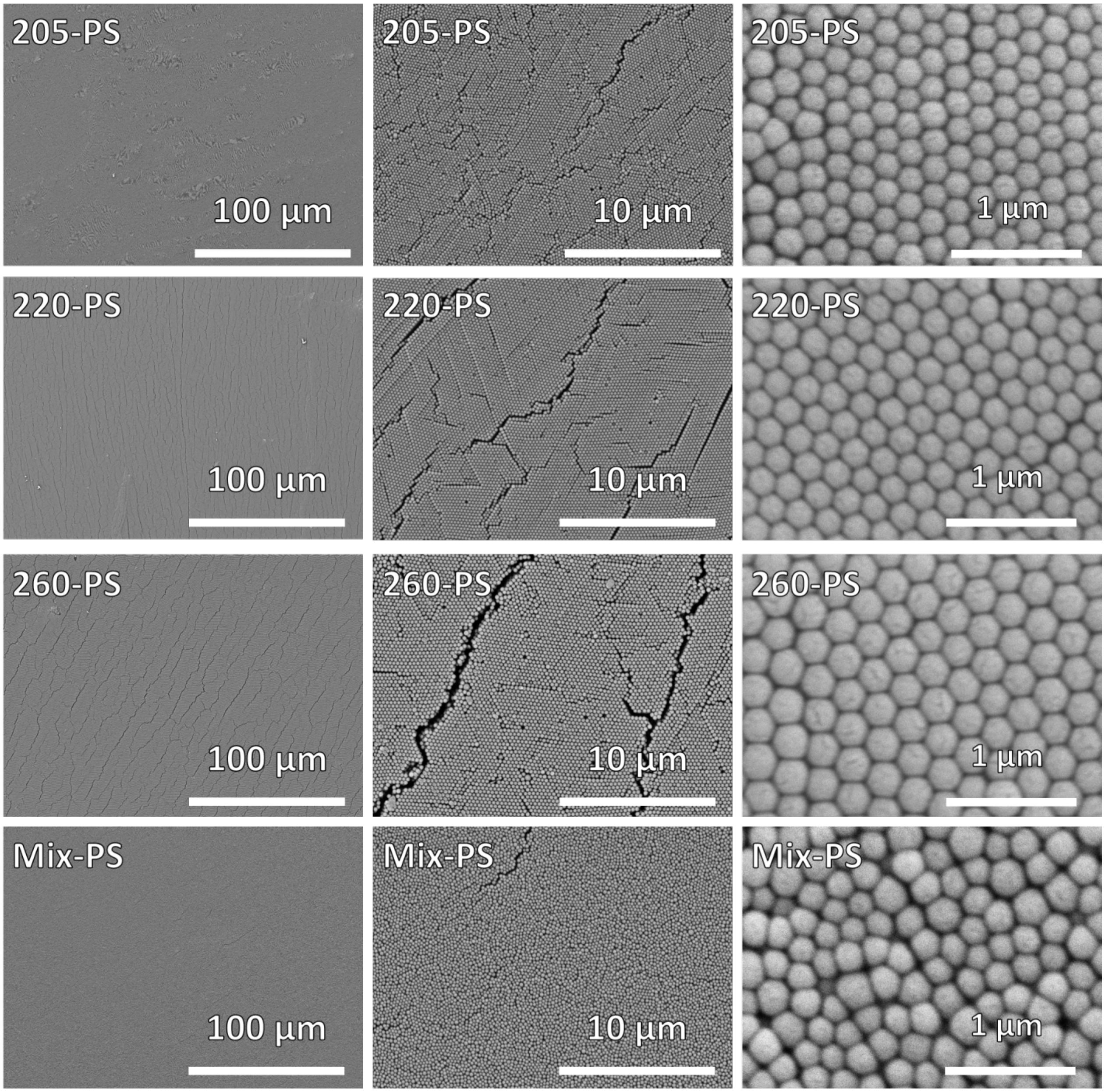

Figure S1: Representative SEM images of 205-PS, 220-PS, 260-PS, and Mix-PS at different magnifications.

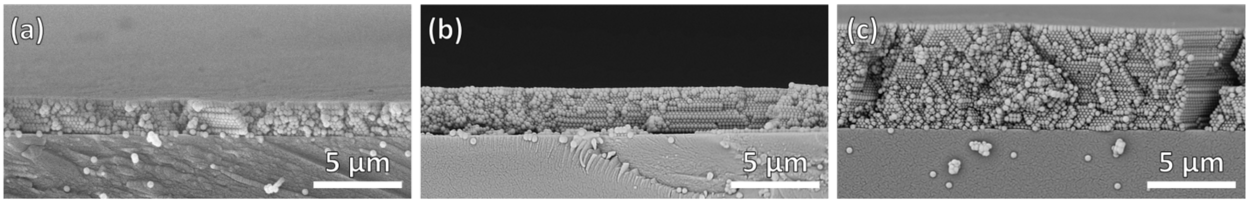

Figure S2: Representative cross-section SEM images of 220-PS with thicknesses of 2 µm (a), 3 µm (b), and 6 µm (c).

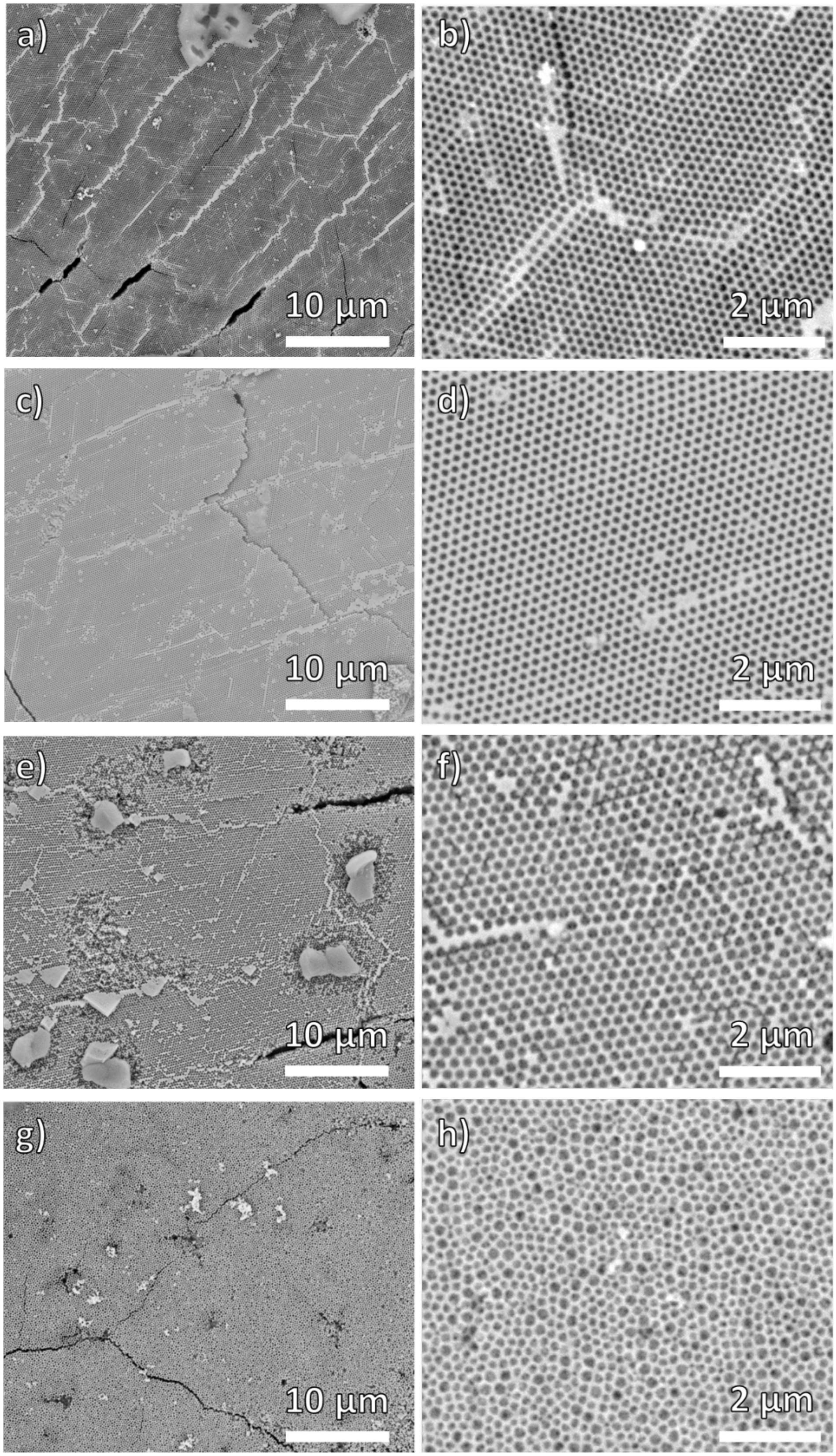

Figure S3: Representative SEM images of 205-$MAPbBr_3$ (a, b), 220-$MAPbBr_3$ (c, d), 260-$MAPbBr_3$ (e, f), and Mix-$MAPbBr_3$ (g, h) at different magnifications.

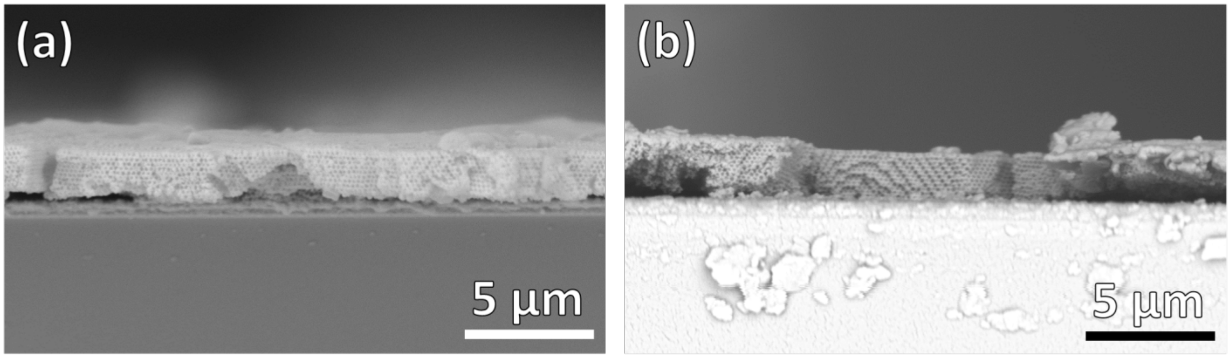

Figure S4: Cross section SEM of 220-$MAPbBr_3$ deposited on FTO (a) and TiO_2 (b).

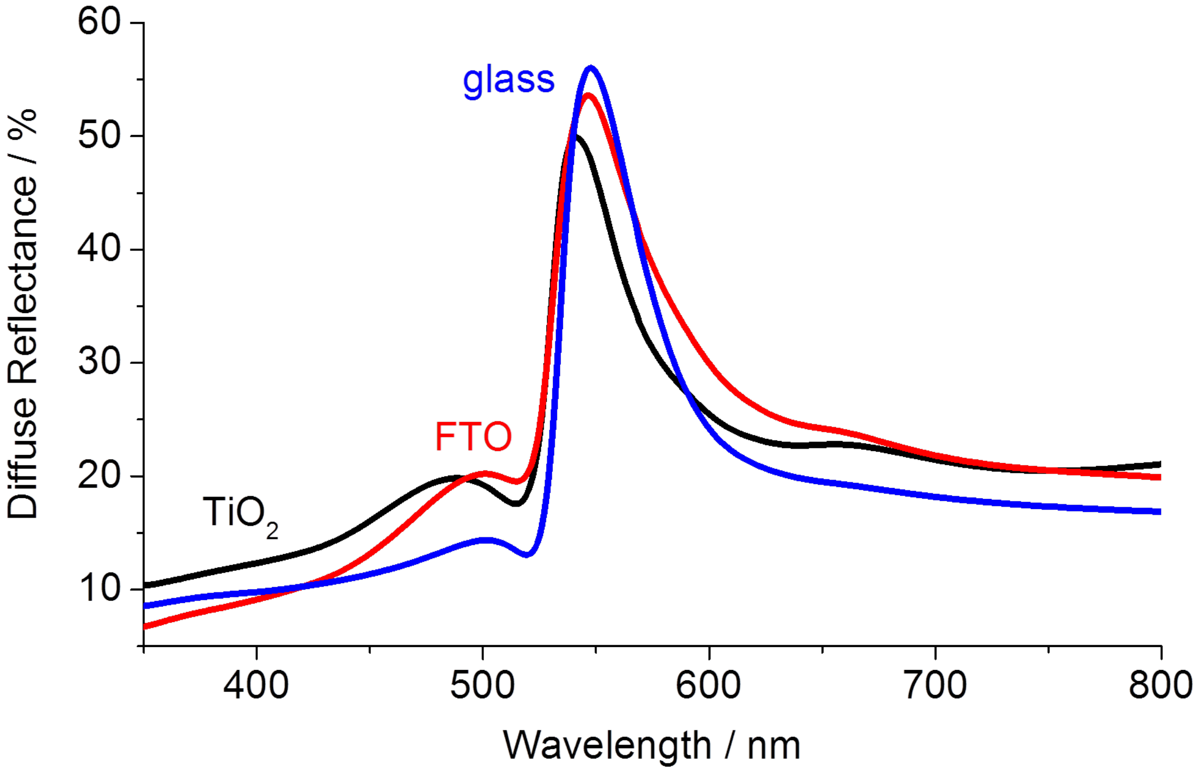

Figure S5: Diffuse reflectance spectrum of 220-$MAPbBr_3$ prepared on glass, FTO, and TiO_2.

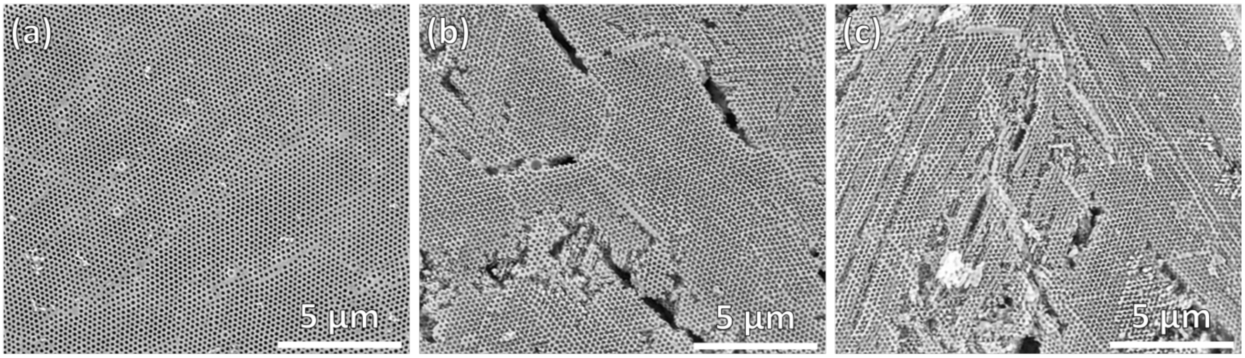

Figure S6: Representative SEM images of 220-$MAPbCl_3$ (a), 220-$MAPbCl_{1.5}I_{1.5}$ (b), and 220-$MAPbI_3$ (c).